Water Research 231 (2023) 119607

Contents lists available at ScienceDirect

Water Research

journal homepage: www.elsevier.com/locate/watres

Photoinduced transformation of ferrihydrite in the presence of aqueous sulfite and its influence on the repartitioning of Cd

Jinwen Qiu [a], Xiaokang Hou [a], Yuan Ren [a], Chengshuai Liu [b], Fangyuan Meng [b], Jyh-Fu Lee [c], Yu-Jung Lin [c], Ziyuan Huang [a], Huanxin Ma [a], Zhenqing Shi [a], Chunhua Feng [a,*]

[a] The Key Lab of Pollution Control and Ecosystem Restoration in Industry Clusters, Ministry of Education, School of Environment and Energy, South China University of Technology, Guangzhou 510006, PR China
[b] State Key Laboratory of Environmental Geochemistry, Institute of Geochemistry, Chinese Academy of Sciences, Guiyang 550081, PR China
[c] National Synchrotron Radiation Research Center, Hsinchu, Taiwan 30076, ROC

ARTICLE INFO

Keywords:
Fe(II) catalysis
Ferrihydrite transformation
Photoinduced reactive species
Cd immobilization
Advanced reduction process
Fe cycle

ABSTRACT

The photoinduced transformation of ferrihydrite is an important process that can predict the geochemical cycle of Fe in anoxic environments as well as the fate of trace elements bonded to Fe minerals. We report that the photooxidation of sulfite by UV irradiation produces hydrated electrons (super-reductants), which significantly promote ferrihydrite reduction to Fe(II), and $SO_3^{\bullet-}$ (a moderate oxidant), enabling its further oxidation to more crystalline Fe(III) products. The experimental results show that the concentration of sulfite was key in influencing the rate and extent of surface-bound Fe(II) formation, which ultimately determined the distribution of individual products. For example, fitting of the Mössbauer spectroscopy data revealed that the relative abundances of mineral species after 8 h of treatment in the UV/sulfite systems were 41.9% lepidocrocite and 58.1% ferrihydrite at 2 mM SO_3^{2-}; 41.8% goethite, 28.2% lepidocrocite, and 29.1% ferrihydrite at 5 mM SO_3^{2-}; and 100% goethite at 10 mM SO_3^{2-}. The combined results of the chemical speciation analysis and the Cd K-edge EXAFS characterization provided compelling evidence that Cd was firmly incorporated into the structure of newly formed minerals, particularly at high sulfite concentrations. These findings provide an understanding of the role of UV/sulfite in facilitating ferrihydrite transformation and promoting Cd stabilization in oxygen-deficit soils and aquatic environments.

1. Introduction

Ferrihydrite is an important product that results from pyrite oxidation in the presence of water and O_2, and it is a natural reservoir for heavy metals due to its relatively large surface area and abundant surface groups (Hiemstra 2013; Liu et al., 2021b; Michel et al., 2007; Shi et al., 2021). Under reducing conditions, ferrihydrite is susceptible to reduction in a biotical or abiotic manner while releasing Fe(II), a reactive species adsorbed on the Fe oxide surface, subsequently inducing its structural transformation to more stable phases, such as lepidocrocite, goethite, magnetite, and hematite (Boland et al., 2014; Hansel et al., 2005; Larsen and Postma 2001; Lovley 1997). This naturally occurring process results in the release of adsorbed heavy metals from the primary hosts and their repartitioning in secondary minerals. For example, Cd-bearing ferrihydrite is subjected to mineral dissolution in the presence of Fe(II), which mobilizes Cd, and it is then immobilized by newly formed Fe(III) (oxyhydr)oxides due to surface binding and structural incorporation (Burton et al., 2019; Yan et al., 2021; Zhao et al., 2022a; Zhou et al., 2020). For several decades, an understanding of the underlying reaction mechanisms and driving forces of this process has attracted considerable attention. Many studies have shown that the reductive dissolution of ferrihydrite in aqueous systems is facilitated by organics either chemically, or more frequently, microbially, by bacteria under the anaerobic conditions (Aeppli et al., 2019; Chen et al., 2015; Dong et al., 2020). In addition, inorganic electron donors, such as sulfide and sulfite, in organic matter-deficient environments are also important contributors to ferrihydrite reduction to Fe(II) (Ma and Banfield 2011; Saalfield et al. 2009; Schoepfer and Lindsay 2022).

The photoinduced reduction of ferrihydrite also plays a crucial role in the Fe cycle of aquatic environments. This process can be achieved through pathways, including i) Fe(III) reduction by photogenerated electrons from Fe(III) (oxyhydr)oxide semiconductors (Lv et al., 2022;

* Corresponding author.
E-mail address: chfeng@scut.edu.cn (C. Feng).

https://doi.org/10.1016/j.watres.2023.119607
Received 30 October 2022; Received in revised form 10 January 2023; Accepted 11 January 2023
Available online 12 January 2023

Shu et al., 2019); ii) Fe(III) reduction by direct ligand-to-metal charge transfer (LMCT) (Kong et al., 2016; Xing et al., 2019); and iii) Fe(III) reduction by indirect reactions with exogenous photoelectrons from coexistent semiconductors or with photoinduced $O_2^{\bullet-}$ from the excitation of photosensitive natural organic matter under aerobic conditions (Shu et al., 2019; Xing et al., 2019). Of particular pertinence to this article is the investigation of the photoinduced reduction of ferrihydrite by hydrated electrons (e_{aq}^-) or hydrogen radicals ($^{\bullet}H$), a photoexcited super-reductant produced from anaerobic environments, which surprisingly receives limited attention in the literature. Based on the knowledge that sulfite stimulated by UV irradiation can produce e_{aq}^-/$^{\bullet}H$ (Chen et al., 2022; Li et al., 2012; Yang et al., 2020b), it is anticipated that this super-reductant can be produced in natural environments containing sulfite. For instance, sulfite is an intermediate species that originates from the microbial oxidation of pyrite (Ma and Banfield 2011; Sim et al., 2017) or the microbial reduction of sulfate (Li and Bao 2021; Lohmayer et al., 2014) in acid mine drainage (AMD) sites. Previous studies have shown that sulfite and other sulfoxy compounds are detectable at the micromolar to millimolar levels in AMD sediments or solutions (Druschel et al., 2004; Ma and Banfield 2011). Moreover, the coexistence of sulfite, ferrihydrite, heavy metals, and UV in AMD-relevant environments is possible because i) the metastable phases of ferrihydrite are also frequently found in the system of pyrite oxidation (Balistrieri et al., 1999; Sánchez España et al. 2005), ii) ferrihydrite generally entraps a variety of heavy metals (i.e., Cd, As, Cr, Pb, Cu, etc.) (Hiemstra 2013; Shi et al., 2021), and iii) solar irradiation can penetrate water in a depth of several meters and sediments with a thickness of several millimeters (Ciani et al., 2005; Liu et al., 2021b). These considerations stimulate in-depth research to understand the behavior of UV/sulfite-induced ferrihydrite dissolution and transformation and its importance to Fe geochemistry and the relevant mobility/immobility of heavy metals.

Therefore, the objectives of the current study were to i) demonstrate the phenomenon that the combination of UV light and aqueous sulfite is conducive to ferrihydrite transformation to more crystalline minerals, which in turn affects the mobility of Cd; ii) elucidate the mechanism governing the reduction dissolution and phase transformation in the UV/sulfite system that is supposed to generate both reductive species (e.g., e_{aq}^-) and oxidative species (e.g., $SO_3^{\bullet-}$ and $^{\bullet}OH$); and iii) identify the evolution of secondary minerals and their interactions with Cd at the molecular level. To achieve these goals, a series of experiments were conducted with and without UV irradiation and in the absence and presence of sulfite at different concentrations. Electron paramagnetic resonance (EPR) and scavenging tests were performed to examine the generation of reactive species and to reveal their roles in ferrihydrite transformation. The extended X-ray absorption fine structure (EXAFS) spectroscopy, Mössbauer spectroscopy, and other physicochemical techniques were used to obtain information regarding the Fe local structure in ferrihydrite and the secondary minerals associated with Cd.

2. Materials and methods

2.1. Chemicals

Ferric chloride hexahydrate ($FeCl_3{\bullet}6H_2O$, >99.0%), cadmium sulfate ($CdSO_4$, >98.0%), sodium sulfite (Na_2SO_3, >98.0%), sodium hydroxide (NaOH, >97.0%), 3-(N-morpholino) propanesulfonic acid (MOPS, >98.5%), 5,5′-dithiobis (2-nitrobenzoic acid) (DTNB, >98.0%), tertiary-butyl alcohol (TBA, >99.5%), methanol (CH_3OH, >99.9%), nitrobenzene (NB, >99.0%), Dimethyl sulfoxide (DMSO, >99.8%) sodium nitrate ($NaNO_3$, >99.0%), sodium nitrite ($NaNO_2$, >99%) and 5,5-dimethyl-1-pyrroline N-oxide (DMPO, >97%) were purchased from Aladdin Industrial Corporation (Shanghai, China). All other reagents were of at least analytical grade and used without further purification. Deionized (DI, 18.2 MΩ cm^{-1}) water was used throughout this study.

2.2. Fe(III) mineral synthesis

Ferrihydrite was synthesized according to the method reported by Schwertmann and Cornell (2008). Briefly, 1 M NaOH was added dropwise to the solution containing 0.1 M $FeCl_3{\cdot}6H_2O$ until its pH was titrated to 7.0–7.5. The resulting particles were centrifuged (8000 rpm, 5 min) and washed 6 times with DI water and then re-dispersed in DI water by ultrasonic shaking. The stock suspension was purged with high-purity N_2 for more than 2 h and then immediately transferred to an anaerobic glove box. The mass concentration of ferrihydrite was calculated from the measured total Fe concentration using the commonly used molecular formula ($Fe_5HO_8{\cdot}4H_2O$). Lepidocrocite was synthesized by oxidizing 600 mL of a 0.2 M $FeCl_2{\cdot}4H_2O$ solution under an air flow rate of 100 mL min^{-1}, when the pH value was maintained at ~6.9 by dropping 2 M NaOH (Schwertmann and Cornell 2008). During this process, the color of the suspension changed from dark greenish-blue to grey and finally to orange. To obtain lepidocrocite, the particles were collected and washed with DI water at least 3 times. Goethite was prepared from an alkaline system (Schwertmann and Cornell 2008), of which 100 mL of 1 M $Fe(NO_3)_3$ was poured into a 2 L polyethylene flask, and 180 mL of 5 M KOH was rapidly added with stirring. The suspension was taken out and held in a closed polyethylene flask at 70 °C for 60 h. After the yellow-brown precipitates were formed during the heating stage, they were centrifuged, washed, and dried to obtain goethite.

2.3. Experimental setup and sampling

All the experiments were carried out under anoxic conditions with 0.5 g L^{-1} ferrihydrite and 5 mg L^{-1} cadmium in a buffer solution (pH 6.8) composed of 50 mM 3-(N-morpholino) propanesulfonic acid (MOPS). Cd and ferrihydrite were equilibrated on a shaking bed in the dark and in the anaerobic glovebox (855-ACB, Plas-Lab, America) for 24 h to ensure adsorption equilibrium. According to the analysis of Visual-MINTEQ, no Cd precipitation was formed under this condition. The sodium sulfite with different concentrations (2, 5, and 10 mM) was added to the suspension, and then the solution pH was adjusted to 6.8 by 6 M NaOH and 1 M H_2SO_4. Quartz tubes of 50 mL were used to hold the suspension. The sealed quartz tubes were taken from the anaerobic glovebox and immediately placed into a photochemical reactor in which the reaction was initiated. The reaction lasted for 8 h at a power of 720 W. The distance between the reaction suspension and the light source (high-pressure mercury lamp) was 6.5 cm. The wavelength of the excitation light irradiated on the reaction system was 300–400 nm, and the light density at the reaction suspension was about 12 mW cm^{-2}. The samples were taken from the photochemical reactor at regular intervals and immediately centrifuged for further chemical analysis. After the centrifugation, the liquid was filtered and collected with a syringe filter (0.22 μm) for the aqueous Cd concentration measurement. The solid was extracted with 10 mL of 0.4 M HCl, and the extractable liquid was chemically analyzed to determine the concentrations of adsorbed Cd and adsorbed Fe(II) (Ford et al., 1997; Frierdich et al., 2014; Reddy et al., 2015). The remaining solid was dissolved by adding 4 mol L^{-1} HCl. After completely dissolving, the liquid was further filtered and collected for an analysis of the content of structurally incorporated Cd. All the experiments were repeated in triplicate, and the average results were recorded throughout the study. The ferrihydrite transformation rate (K) was estimated from the following equation (Maillot et al., 2011; Michel et al., 2007; Zhao et al., 2022a; Zhou et al., 2020).

$$K = -\frac{\ln\left\{[\mathrm{Fe(III)}]_{ex}/[\mathrm{Fe(III)}]_t\right\}}{t} \quad (1)$$

where $[Fe(III)]_{ex}$ is the concentration of 0.4 M HCl-extracted Fe(III) regarded as the content of unconverted ferrihydrite (Ford et al., 1999; Schwertmann and Cornell 2008; Zhao et al., 2022b), $[Fe(III)]_t$ refers to the total Fe(III) concentration in the solid extracted by 4 M HCl, and t

stands for the reaction time (h).

2.4. Characterization and analysis

The contents of Fe (II) and total Fe in the aqueous samples were quantified using the Ferrozine analysis. For the determination of dissolved Cd, the sample was diluted with 2% HNO_3, stored at 4 °C, and analyzed using an atomic absorption spectrometer (AAS, PinAAcle 900T, PerkinElmer, USA). The detection of limit of AAS for Cd was 2 μg L^{-1}. The concentration of S(IV) was monitored using the modified 5,5′-dithiobis (2-nitrobenzoic acid) colorimetric method with a UV–vis spectrophotometer (UV-2550, Shimadzu, Kyoto, Japan). The details for S(IV) concentration measurement are presented in Text S1. Prior to the physicochemical characterizations, the solid products were collected with a syringe filter (0.22 μm), freeze-dried, and stored in a refrigerator at 4 °C if the test apparatuses were not immediately available (this storage method has been widely reported in previous studies (Boland et al., 2014; Shu et al., 2019)). Otherwise, the freeze-dried samples were promptly detected. We should state that the phase transformation of the resultant minerals during storage did not occur because they were in the form of Fe(III) (oxyhydr)oxides. The surface morphology of the solid samples was characterized using scanning electron microscopy (SEM, Merlin, Zeiss Co., Germany). The mineral phases of the selected solid samples were analyzed using an X-ray diffractometer (X'Pert PRO MRD, PANalytical, Holland, Germany) and Cu Kα radiation (λ = 1.5418 Å, 40 kV, and 40 mA). Diffractograms were recorded in the 2θ range of 10−70° with a step size of 0.02° at a scanning rate of 2° min^{-1}. The Fourier transform infrared spectra (FTIR, VERTEX 33, Bruker, Germany) were collected in the absorbance mode in the range of 450–4500 cm^{-1} with a spectral resolution of 4 cm^{-1}. The electron paramagnetic resonance (EPR) spectra were collected on a Bruker EMX A300-10/12 (Germany) spectrometer. The Mössbauer spectra were collected at 13 K in the transmission mode on a WSS-10 Mössbauer spectrometer (WissEL GmbH, Germany) equipped with a closed cycle cryostat (SHI-850, Janis Research Co., Wilmington, MA, USA). The velocity scale of the Mössbauer spectra was calibrated with reference to α-iron. The X-ray absorption spectra (XAS) of Fe and Cd K-edges were collected in the transmission and fluorescence mode, and conducted at beamline BL17C and beamline BL01C of the Taiwan Light Source (TLS), respectively. The obtained XAFS data were processed in Athena (version 0.9.26) for background, pre-edge line, and post-edge line calibrations. More detailed parameters for collecting the XAFS data and the corresponding analysis are depicted in Text S2.

3. Results and discussion

3.1. Characterizations of the structural evolution of the UV/sulfite-induced transformation of Cd-bearing ferrihydrite

The XRD analysis was conducted to discern the variation in the crystallized structure of Cd-bearing ferrihydrite upon UV irradiation and the addition of aqueous sulfite, which influences the rate and extent of

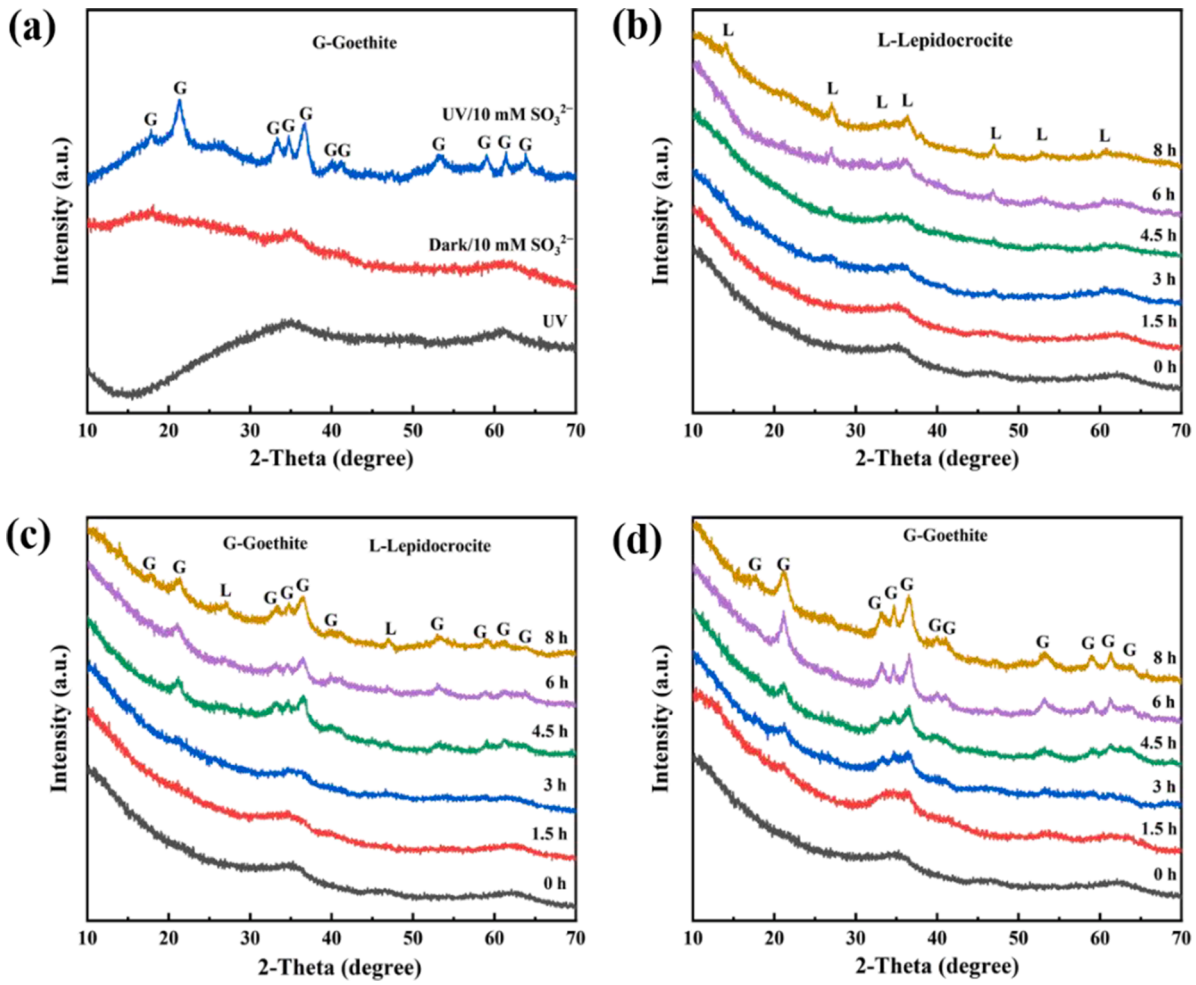

Fig. 1. (a) XRD patterns of the solid phases resulting from the 8-h transformation of Cd-loaded ferrihydrite under different conditions. Time-dependent XRD patterns of the solid phases resulting from the transformation of Cd-loaded ferrihydrite upon UV irradiation in the presence of (b) 2, (c) 5, and (d) 10 mM SO_3^{2-}. Experimental conditions: [ferrihydrite] = 0.5 g L^{-1}, [Cd^{2+}] = 5 mg L^{-1}, and pH = 6.8.

ferrihydrite transformation and the resulting products. Fig. 1a shows that the diffraction peaks of 2-line ferrihydrite (typically at 2θ of ~33° and ~61°) displayed no detectable changes under the conditions of either UV alone or 10 mM SO_3^{2-} alone. In stark contrast, the combination of UV and sulfite after 8 h of aging induced the appearance of strongly crystalline peaks attributed to goethite (PDF#00-29-0713) (Sheng et al., 2020a), signifying the interactive effect in promoting ferrihydrite transformation. The occurrence of ferrihydrite transformation is closely linked to the concentration of sulfite and is dependent on the reaction time. At a low concentration (2 mM SO_3^{2-}), the transformation exhibited slower overall kinetics and resulted in the formation of lepidocrocite (PDF#00-08-0098) (Sheng et al., 2020a); for instance, the distinct emergence of the lepidocrocite peaks was observed until 8 h of reaction time (Fig. 1b). When the concentration of SO_3^{2-} increased to 5 mM, obvious changes in the peak profile appeared at 6 h, and the final product at 8 h was composed of goethite (major) and lepidocrocite (minor) (Fig. 1c). Fig. 1d reveals that increasing the sulfite concentration to 10 mM significantly enhanced the transformation kinetics, as 3 h of reaction time led to a remarkable appearance of new diffraction peaks, which were attributed to goethite. These findings are in good agreement with the literature results regarding the Fe(II)-catalyzed ferrihydrite transformation into secondary and more crystalline minerals (Boland et al., 2014; Liu et al., 2007; Pedersen et al., 2005). The production rate of adsorbed Fe(II) and the subsequent oxidation rate of this species are believed to be the key factors determining the type of secondary minerals and the extent of their formation (this point is discussed in later sections).

The difference in the functional groups of Fe (oxyhydr)oxides before and after treatment by UV/sulfite was explored using the FTIR, which also supported the dynamic evolution of the mineral phase. In general, the strong bands centered at ~795 and ~890 cm^{-1} together with a broad band at ~640 cm^{-1} were attributed to the FTIR spectra of goethite (Gotić and Musić 2007; Kahani and Jafari 2009). Lepidocrocite exhibits three bands at ~554, ~740, and ~ 1021 cm^{-1}, corresponding to the Fe–O, γ_{OH} out-of-plane, and δ_{OH} in-plane vibrations, respectively (Lewis and Farmer 1986; Xiao et al., 2017). Fig. 2a clearly indicates that there was little change in the infrared spectra under the UV alone and dark/sulfite conditions and that the characteristic features derived from goethite were visible in the sample after 8 h of treatment. Note that the absorption peaks at 1040 cm^{-1} were due to the existence of S-O

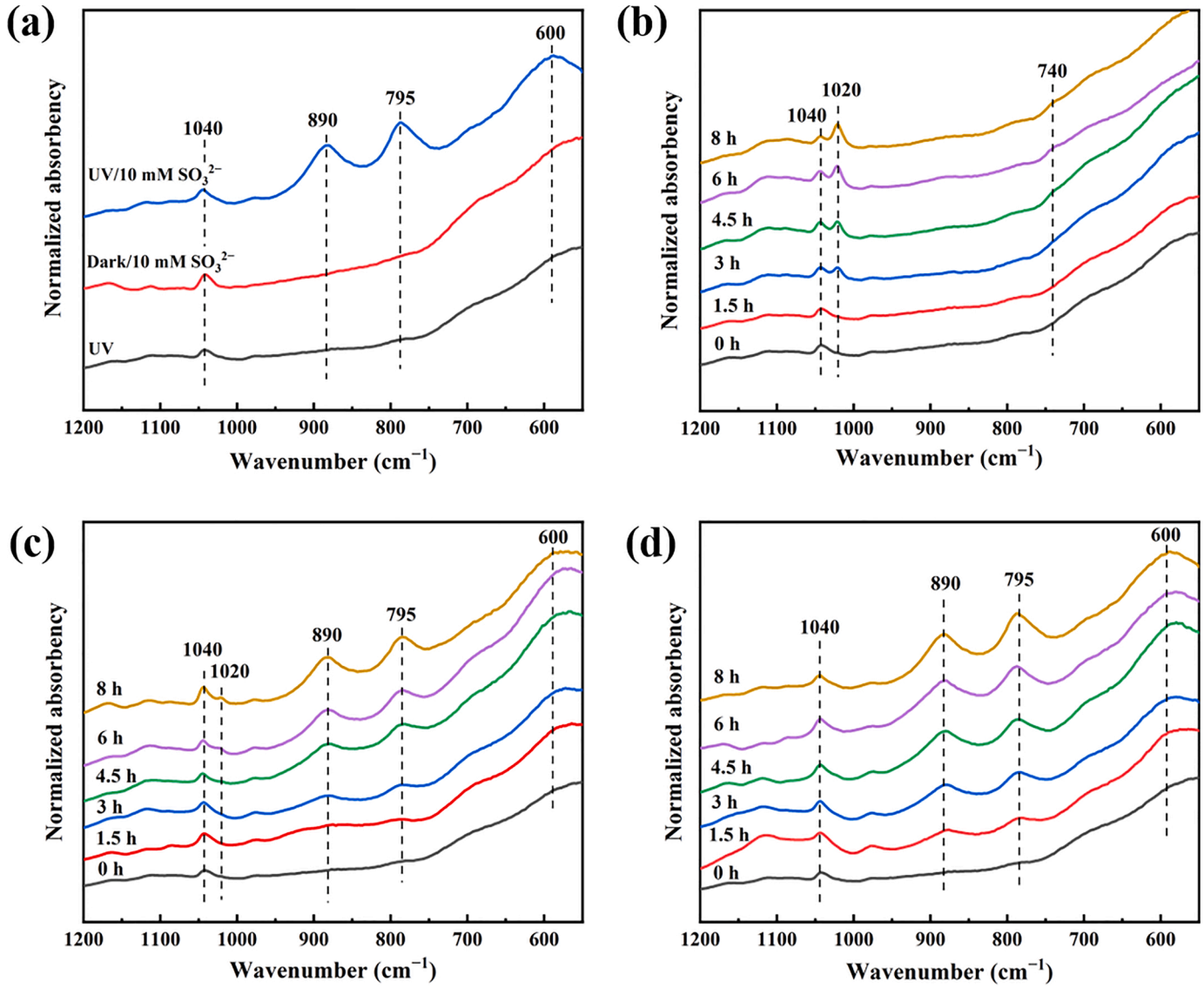

Fig. 2. (a) FTIR spectra of the solid phases resulting from the 8-h transformation of Cd-loaded ferrihydrite under different conditions. Time-dependent FTIR spectra patterns of the solid phases resulting from the transformation of Cd-loaded ferrihydrite upon UV irradiation in the presence of (b) 2, (c) 5, and (d) 10 mM SO_3^{2-}. Experimental conditions: [ferrihydrite] = 0.5 g L^{-1}, [Cd^{2+}] = 5 mg L^{-1}, and pH = 6.8.

stretching of sulfur-containing group in the buffer solution (Zhou et al., 2022). As illustrated in Fig. 2b, the addition of 2 mM SO_3^{2-} to the UV system provoked the appearance of typical bands assigned to lepidocrocite from 3 to 8 h of operation, and their intensities increased over time. The presence of 5 mM SO_3^{2-} led to a gradual emergence of characteristic bands corresponding to goethite, which accompanied the formation of the lepidocrocite bands (Fig. 2c). Fig. 2d shows that the predominant bands were attributed to goethite in the UV system containing 10 mM SO_3^{2-}. The vibration peaks were strengthened with prolonged time, suggesting that the elevated amount of goethite formed over time. It should be emphasized that the uptake of Cd (~10 mg g^{-1} at an initial Cd concentration of 5 mg L^{-1}) in the ferrihydrite did not visibly impact its transformation, as is evident based on the observations that the time-dependent XRD and FTIR results of the ferrihydrite samples in the absence of Cd were highly similar to those in the presence of Cd (Fig. S1).

The SEM analysis was performed to examine the differences in the mineral surface morphology during the phase transformation. Fig. S2 shows the SEM images of the as-synthesized Cd-bearing ferrihydrite and the end-products of the transformation under UV irradiation with the sulfite concentrations of 0, 2, 5, and 10 mM. When sulfite was unavailable, the solid surface appeared to be flocculent, which resembled that of the initial ferrihydrite, again supporting the role of sulfite in promoting phase transformation. The SEM image of the sample formed at 2 mM SO_3^{2-} exhibited a typical lamellar structure of lepidocrocite (Qafoku et al., 2020; Schwertmann and Cornell 2008). Both lamellar and needle-like crystals were observed on the mineral surface after the reaction in the UV/sulfite system with 5 mM SO_3^{2-}. The addition of 10 mM made the needle-like crystals prevalent on the surface, conforming to the generation of goethite as the ultimate product of the Fe(II)-catalyzed ferrihydrite transformation (Boland et al., 2014; Hansel et al., 2005).

A further understanding of the mineral transformation of Cd-bearing ferrihydrite at the molecular level was aided by the Mössbauer spectroscopy and the Fe K-edge EXAFS spectroscopy characterizations. Remarkable variations in the Mössbauer spectra (Figs. 3a–d) were revealed between the samples after UV irradiation over 8 h and in the absence and presence of sulfite at different concentrations, which is in good agreement with the XRD and FTIR results. The fitting results and relevant parameters are provided in Table S1. The Mössbauer spectrum of the mineral without the engagement of sulfite exhibited a six-fold peak with the typical parameters of ferrihydrite (IS = 0.46 mm s^{-1}, QS = −0.05 mm s^{-1}) (Bishop et al., 1993). The addition of 2 mM SO_3^{2-} led to a partial transformation of ferrihydrite into lepidocrocite (IS = 0.42 mm s^{-1}, QS = −0.037 mm s^{-1}), and the addition of 5 mM SO_3^{2-} yielded the appearance of secondary minerals, including lepidocrocite (IS = 0.52 mm s^{-1}, QS = −0.01 mm s^{-1}) and goethite (IS = 0.48 mm s^{-1}, QS = −0.13 mm s^{-1}). Increasing the concentration of SO_3^{2-} to 10 mM resulted in a complete ferrihydrite transformation to goethite (IS = 0.44 mm s^{-1}, QS = −0.22 mm s^{-1}) (Bishop et al., 1993; Meng et al., 2022; ThomasArrigo et al., 2018). The relative abundances of the mineral species after illumination for 8 h in the aqueous sulfite solution were estimated from the fitting results: 41.9% lepidocrocite and 58.1% ferrihydrite at 2 mM SO_3^{2-}; 41.8% goethite, 28.2% lepidocrocite, and 29.1% ferrihydrite at 5 mM SO_3^{2-}; and 100% goethite at 10 mM SO_3^{2-}. Beyond the solid-phase Fe(III) signals, the peaks associated with adsorbed Fe(II) were also observed in the original spectra of samples with 5 and 10 mM SO_3^{2-}. The relative content of adsorbed Fe(II) increased with the increasing sulfite concentration from 0.95% (5 mM SO_3^{2-}) to 4.46% (10 mM SO_3^{2-}) (Liu et al., 2021a). This indicates that the enhanced concentration of Fe(II) bound to the mineral is favorable to ferrihydrite conversion into goethite (Boland et al., 2014; Huang et al., 2021; Jones et al., 2017).

The Fe K-edge EXAFS spectra also provide solid evidence of successful ferrihydrite transformation in the UV/sulfite systems and a dependence of the conversion proportion on the sulfite concentration. As illustrated in Fig. 3e, a negligible transformation of ferrihydrite occurred under the sulfite-free condition with UV radiation after 8 h of reaction time. Likewise, no conversion appeared with the addition of 10 mM SO_3^{2-} in the dark. On the contrary, the Fe K-edge EXAFS signals clearly changed in the UV/sulfite solution. Based on the fitting results by referring to the standard curves of ferrihydrite, lepidocrocite, and goethite, the phase fractions of these minerals in different solid samples after 8 h of radiation were quantified (Fig. 3f). Specifically, the proportions of ferrihydrite were 63.5%, 29.0%, and 0, those of lepidocrocite were 36.5%, 21.7%, and 0, and those of goethite were 0, 49.3%, and 100%, corresponding to the as-resulted solids under UV irradiation with 2, 5, and 10 mM SO_3^{2-}, respectively. Despite the slight differences in the exact values between the fitted results of EXAFS and the Mössbauer analysis, they displayed an identical trend, with lepidocrocite as the intermediate product at a low sulfite concentration and goethite as the final product at a high sulfite concentration. This behavior is similar to that reported for the transformation of Fe(III) oxides assisted by biogenic Fe(II) (Xiao et al., 2018).

3.2. *Mechanistic investigations on UV/sulfite-induced ferrihydrite transformation*

It has been documented that the rate of Fe(II) uptake and the solid-bound Fe(II) concentration are important in determining which particular minerals form (and at what rate) with respect to Fe(II)-accelerated ferrihydrite transformation to more crystalline products (Boland et al., 2014; Liu et al., 2021a; Sheng et al., 2020b). Likewise, the time courses of adsorbed Fe(II) concentrations in all setups were recorded, and their dependence on the initial sulfite concentration was evaluated. Fig. 4a shows that the rate and extent of solid-associated Fe(II) formation were closely linked with the content of sulfite. No solid-associated Fe(II) was detectable in the absence of sulfite, suggesting that no other reductants responsible for Fe(III) reduction were available in such systems. A more rapid increase in the concentration of adsorbed Fe(II) was observed at 10 mM SO_3^{2-}, and it mounted to the summit (9.02 mg L^{-1}) within 20 min. The relevant values associated with 5 and 2 mM SO_3^{2-} distinctly decreased to 6.25 and 3.33 mg L^{-1}, respectively. The order of the adsorbed Fe(II) concentration determined by the wet chemistry analysis was highly consistent with the results revealed by the Mössbauer analysis. The latter suggested relatively higher adsorbed Fe(II) values, particularly at 10 mM SO_3^{2-}, possibly due to the involvement of adsorbed Fe(II) and structural Fe(II) in the mineral.

It is expected that the reduction and dissolution of ferrihydrite were driven by hydrated electrons (e_{aq}^-), photoexcited super-reductants ($E \leq$ −2.3 V vs. NHE) arising from the UV/sulfite process (Li et al., 2012; Wacławek et al., 2022). To confirm the effectiveness of e_{aq}^- in promoting Fe(III) reduction, the EPR analysis and scavenging experiments were conducted. Distinct TEMPO-e_{aq}^- signals were observable (Fig. 4b) in UV/sulfite, whose intensities were significantly attenuated upon the addition of ferrihydrite after 1 min of irradiation. Increasing the operation time to 3 min completely extinguished the EPR signals. Both NO_3^- and NO_2^- were selected as the quencher for e_{aq}^- due to the extremely high rate constants of 9.7×10^9 and 4.1×10^9 M^{-1} s^{-1}, respectively (Buxton et al., 1988; Wang et al., 2022). Fig. 4c shows that the rate of ferrihydrite transformation was 0.115 h^{-1} in the UV system with 10 mM SO_3^{2-} and that the presence of NO_3^- and NO_2^- greatly inhibited the conversion of ferrihydrite. These results corroborate the role of e_{aq}^- in facilitating Fe (III) reduction.

It can also be observed in Fig. 4a that the adsorbed Fe(II) concentration first climbed and then dropped with the increasing time in the UV/sulfite systems. This profile indicates that Fe(II) oxidation accompanied the UV/sulfite-induced reduction of ferrihydrite, which is in accordance with the observation of microbial ferrihydrite reduction (Dong et al., 2020). Previous studies have demonstrated that Fe(II)–Fe (III) electron transfer at the iron oxide–water interface occurs, which accounts for the ultimate mineral transformation when additional Fe(II) was reacted with ferrihydrite (Boland et al., 2014; Handler et al., 2009).

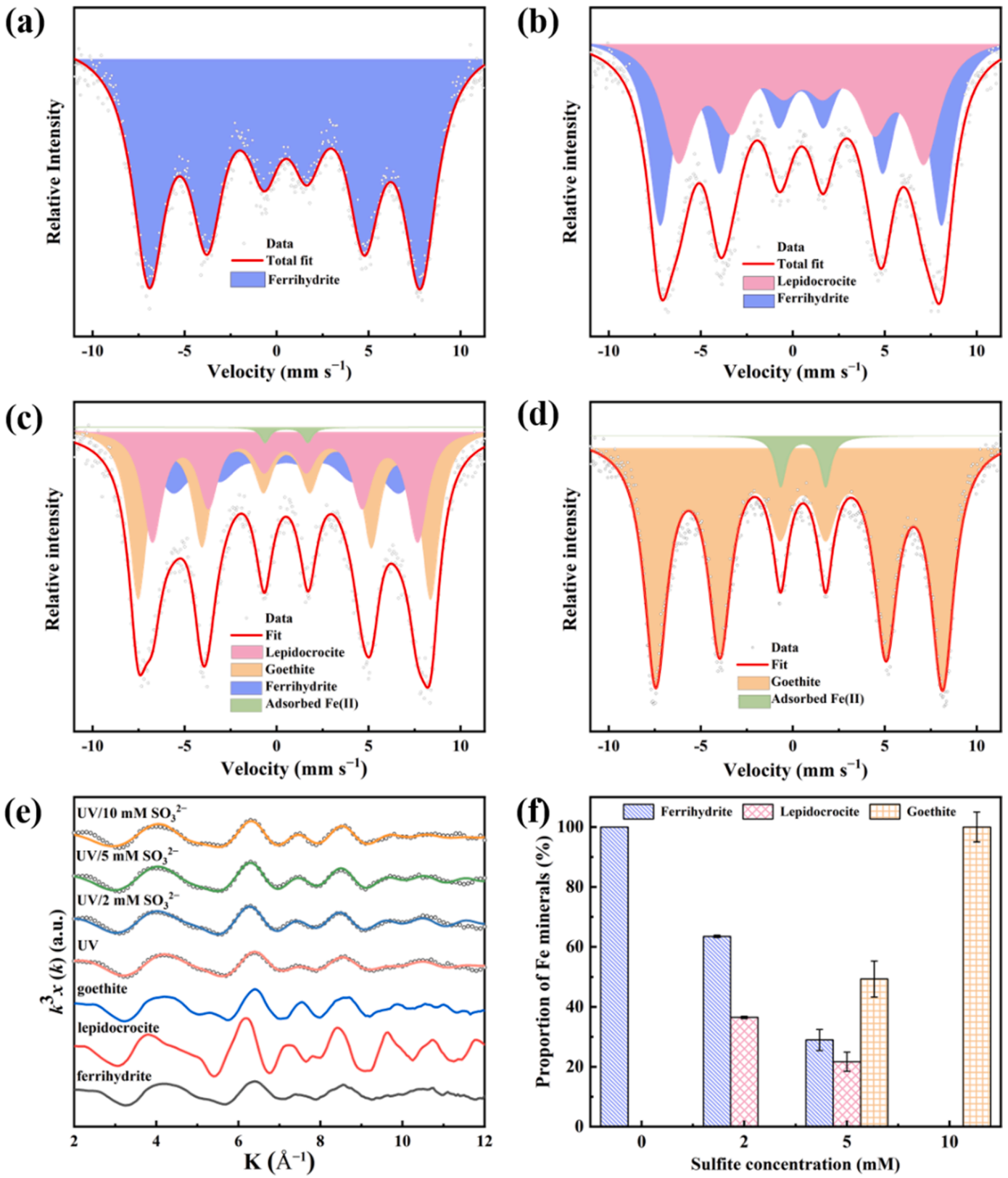

Fig. 3. Mössbauer spectra (13 K) and fitting results of the solid phases resulting from the transformation of Cd-loaded ferrihydrite upon UV irradiation in the presence of (a) 0, (b) 2, (c) 5, and (d) 10 mM SO_3^{2-}. (e) Fe K edge EXAFS spectra and (f) the corresponding linear combination fitting results of the solid phases resulting from the UV/sulfite systems at different sulfite concentrations. Experimental conditions: [ferrihydrite] = 0.5 g L^{-1}, [Cd^{2+}] = 5 mg L^{-1}, pH = 6.8, and reaction time = 8 h.

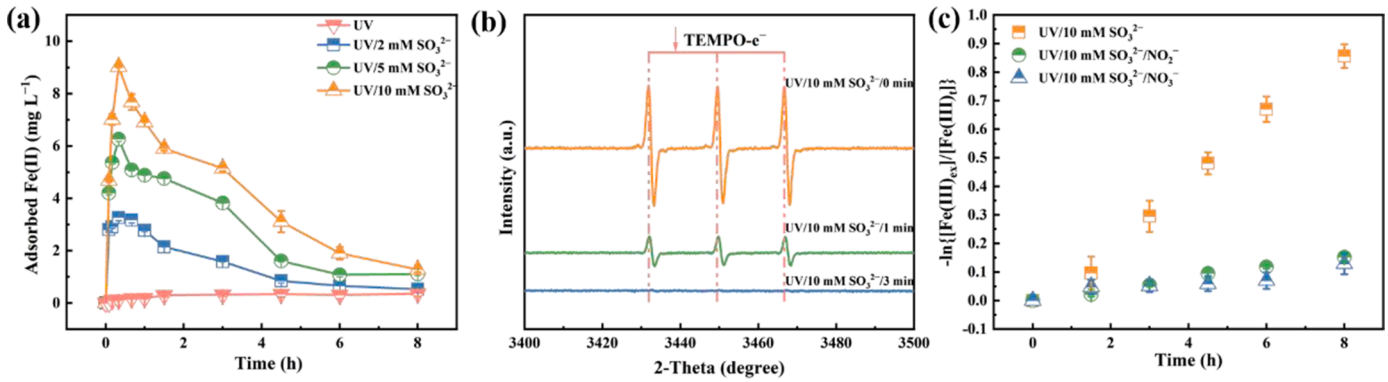

Fig. 4. (a) Time courses of the adsorbed Fe(II) concentration in the UV/sulfite systems at different sulfite concentrations. (b) Time-dependent TEMPO-probed EPR spectra of hydrated electron (e_{aq}^-) in the UV/sulfite system containing 10 mM SO_3^{2-}. (c) Temporal changes in the Cd(II)-loaded ferrihydrite transformation rates with different scavengers. Experimental conditions: [ferrihydrite] = 0.5 g L^{-1}, [Cd^{2+}] = 5 mg L^{-1}, [TEMPO] = 200 μM, [scavenger] = 20 mM, and pH = 6.8.

For this Fe(II)-catalyzed process, the concentration of adsorbed Fe(II) is usually maintained at a relatively constant value (Sheng et al., 2020b); however, in our case, the content of solid-associated Fe(II) substantially decreased with the increase in the duration (e.g., from 9.0 mg L^{-1} at 20 min to 1.3 mg L^{-1} at 8 h). It thus can be hypothesized that an alternative pathway should influence the oxidation of Fe(II) and the resulting Fe(III) (oxyhydr)oxide products. To verify this, a series of reference experiments were performed with the addition of external Fe(II) at different concentrations to the aqueous ferrihydrite systems. Fig. S3 illustrates that the levels of adsorbed Fe(II) were comparable to those in the UV/sulfite processes, but they did not significantly vary during 8 h of operation. Despite the observations of ferrihydrite transformation, lepidocrocite appeared to be the major crystalline mineral for all the investigated cases with an adsorbed Fe(II) concentration that varied from 3.0 to 10.5 mg L^{-1}, as shown by the XRD results (Fig. S4). This is different from the result that goethite was the predominant product in the UV/sulfite systems at high sulfite concentrations. Moreover, the presence of sulfite (10 mM SO_3^{2-}) without the involvement of UV can result in the reduction of ferrihydrite (evidenced by the release of Fe(II) and its adsorption on the solid surface, as shown in Fig. S5), but it was ineffective in causing its conversion (Fig. 1a). This implies the importance of other possible oxidants having the capacity to convert Fe(II) into Fe(III).

Fig. 5a depicts the DMPO-relevant EPR signals detected in different systems, which are suggestive of the presence of $SO_3^{\bullet-}$, another product resulting from the photolysis of sulfite (Li et al., 2012; Yang et al., 2020a). The UV/sulfite system exhibited the strongest DMPO-$SO_3^{\bullet-}$ intensities, and the co-existence of ferrihydrite alleviated the magnitude, indicating the consumption of $SO_3^{\bullet-}$ likely by Fe(II). The addition of more amounts of Fe(II) further weakened the signals; this proves the involvement of $SO_3^{\bullet-}$ in Fe(II) oxidation. In addition, Fig. S6 shows that no relevant signals were visible under the dark condition and that the intensities of the DMPO-$SO_3^{\bullet-}$ patterns were positively correlated with the initial sulfite concentration. The possibility of a reaction between $SO_3^{\bullet-}$ and Fe(II) was also evident based on the differentiation in the decay rate of sulfite between the aqueous systems in the presence and absence of ferrihydrite. As illustrated in Fig. 5b, the addition of ferrihydrite remarkably retarded the decline in the sulfite concentration, and this inhibition effect was distinct for all the investigated systems. These results are considered to be the regeneration of sulfite resulting from $SO_3^{\bullet-}$-induced Fe(II) oxidation. It should be noted that no DMPO-HO$^\bullet$ patterns were revealed in the UV/sulfite system, corroborating that insignificant amounts of HO$^\bullet$ were produced upon light irradiation. Fig. 5c also shows that the addition of NB, MeOH, and TBA, excellent scavengers preferentially reacting with HO$^\bullet$ (Huang et al., 2017; Liang et al., 2020), did not alter the rate of ferrihydrite transformation, which is indicative of a negligible role of HO$^\bullet$ in Fe(II) oxidation. High-valence Fe species with a high oxidative capacity may be produced from the Fe (II)-catalyzed Fe(III) mineral transformation system under anoxic conditions (Hua et al., 2022); however, the addition of DMSO that can quench Fe(IV) species (Liang et al., 2020) apparently did not slow the conversion rate (Fig. 5c), suggesting that Fe(IV) also has an inappreciable impact on Fe(II) oxidation.

To summarize, the UV/sulfite process-initiated ferrihydrite transformation primarily involves two reaction steps: (i) reduction and dissolution of Fe(III) at the ferrihydrite surface and (ii) uptake of Fe(II) by the solid and its subsequent oxidation to Fe(III). For the first step, the photolysis of sulfite yields the formation of e_{aq}^- and $SO_3^{\bullet-}$ (Eq. (2)) (Li et al., 2012); the former species is a powerful reductant that triggers the reduction of surface-bound Fe(III) to Fe(II) (Eq. (3)). A similar Fe(III)

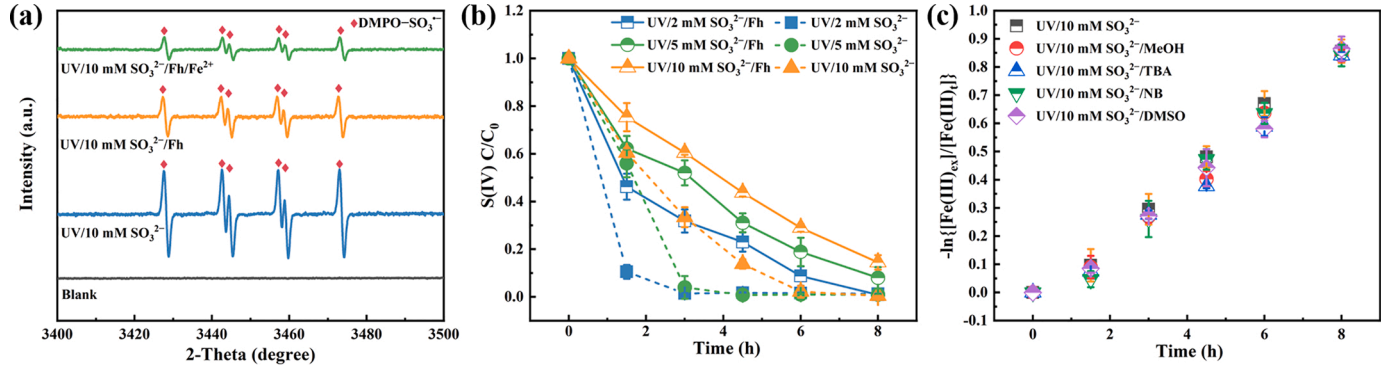

Fig. 5. (a) DMPO-probed EPR spectra of different systems. (b) Time courses of the S(IV) concentration in the UV/sulfite systems at different sulfite concentrations with or without the involvement of ferrihydrite (Fh). (c) Temporal changes in the Cd(II)-loaded ferrihydrite transformation rates with different scavengers. Experimental conditions: [ferrihydrite] = 0.5 g L^{-1}, externally added [Fe^{2+}] = 2 mM, [Cd^{2+}] = 5 mg L^{-1}, [DMPO] = 100 mM, [scavenger] = 10 mM, and pH = 6.8.

reduction can also be driven by sulfite itself (Eq. (4)), despite its relatively lower reducing capacity. For the second step, it is generally accepted that the electron transfer−atomic exchange mechanism (Eqs. (5) & (6)) governs Fe(II) oxidation and recrystallization (Boland et al., 2014; Sheng et al., 2020b); however, in our cases, the contribution of $SO_3^{\bullet-}$-induced conversion of Fe(II) (Eq. (7)) should play a crucial role in the oxidation of surface-bound Fe(II) to newly formed Fe(III) oxyhydroxides. This reaction is thermodynamically favorable considering the higher value of $E(SO_3^{\bullet-}/SO_3^{2-})$ (0.63 V vs. SHE) than that of E(≡Fe(III)/≡Fe(II)) (~ −0.18 vs. SHE) (Liu et al., 2020). It should be stated that sulfite binding to the surface of ferrihydrite is a prerequisite step for e_{aq}^--triggered Fe(III) reduction and $SO_3^{\bullet-}$-induced Fe(II) oxidation process, because all the reactions are considered to take place at the surface. The adsorption of sulfite by ferrihydrite was evident from the prominent FTIR peaks (e.g., at ~1040 cm^{-1} in Fig. S7) that were assigned to S-O stretching of sulfur-containing group (Faguy et al., 1996). Moreover, an increase in the sulfite concentration led to the increasing intensity of the characteristic peaks. Previous studies have also reported that sulfite can bind to Fe(III) via inner-sphere complexation (Zhou et al., 2018). The rate and extent of surface-bound Fe(II) formed upon UV irradiation increased with the increase in the initial sulfite concentration, ultimately determining the type of secondary minerals and at what rate they formed. Lepidocrocite production dominated at relatively low surface-associated Fe(II) concentrations, whereas goethite production was predominant at high surface-associated Fe(II) concentrations. The acceleration of ferrihydrite transformation and goethite formation was achieved by the elevated sulfite concentration.

$$SO_3^{2-} + h\nu \rightarrow SO_3^{\bullet-} + e_{aq}^- \quad (2)$$

$$\equiv Fe(III) + e_{aq}^- \rightarrow \equiv Fe(II) \quad (3)$$

$$\equiv 2Fe(III) + SO_3^{2-} + H_2O \rightarrow 2\equiv Fe(II) + SO_4^{2-} + 2H^+ \quad (4)$$

$$\equiv Fe(III)OFe(II)^+ \rightarrow \equiv Fe(II)OFe(III)^+ \quad (5)$$

$$\equiv Fe(II)OFe(III)^+ + H^+ \rightarrow \equiv Fe(III)OH_{new} + \equiv Fe(II) \quad (6)$$

$$SO_3^{\bullet-} + \equiv Fe(II) \rightarrow SO_3^{2-} + \equiv Fe(III)_{new} \quad (7)$$

3.3. Repartitioning of Cd upon UV/sulfite-induced ferrihydrite transformation

Ferrihydrite is a natural sink for Cd(II) in soils and aquatic environments due to its relatively high surface area and abundant surface

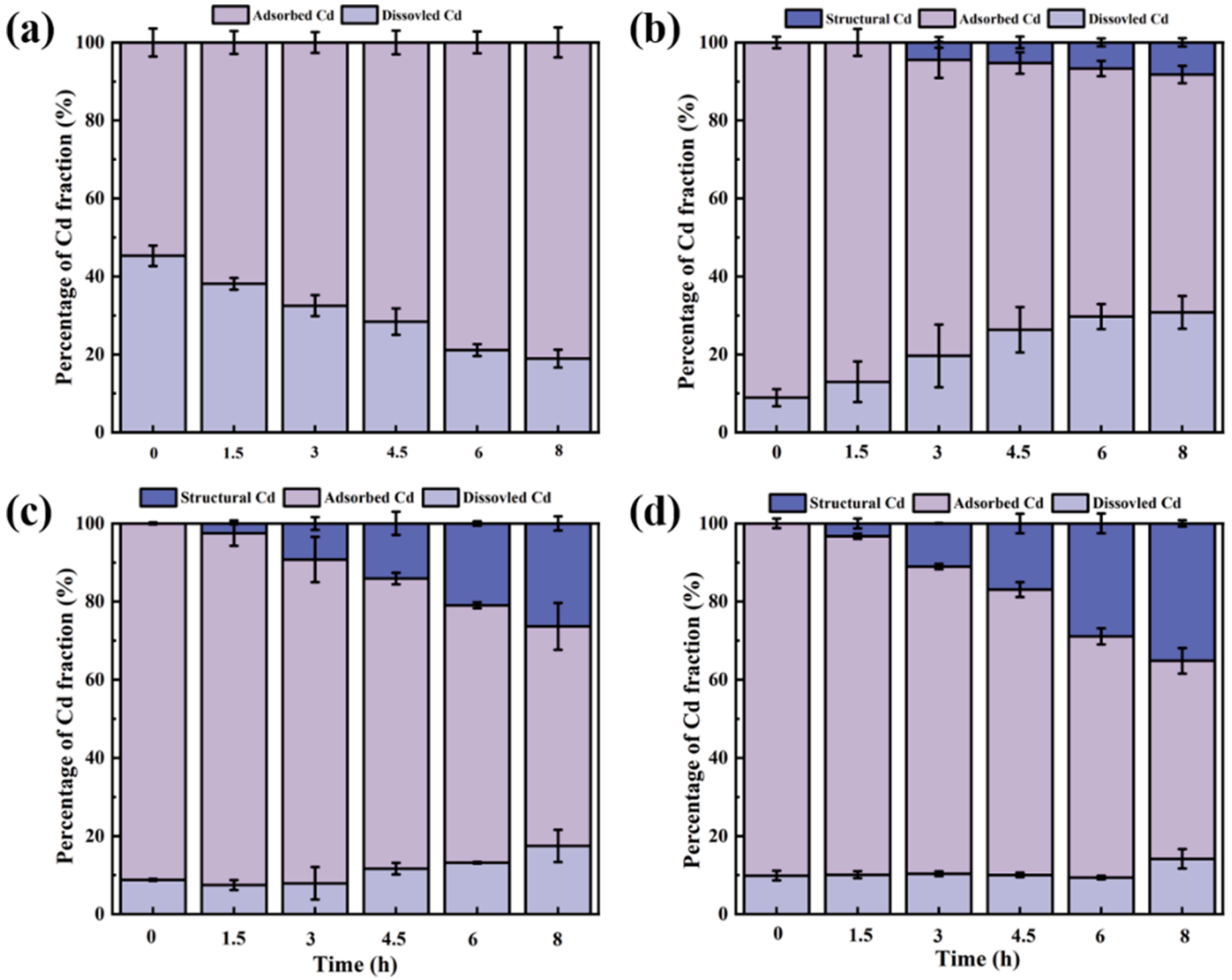

Fig. 6. Temporal changes in the Cd distribution determined by the extraction experiments in the UV/sulfite systems containing (a) 0, (b) 2, (c) 5, and (d) 10 mM SO_3^{2-}. Experimental conditions: [ferrihydrite] = 0.5 g L^{-1}, [Cd^{2+}] = 5 mg L^{-1}, and pH=6.8.

hydroxyl groups, and the transformation of ferrihydrite to more crystalline minerals significantly influences the speciation and mobility of Cd (Maillot et al., 2011; Michel et al., 2007; Zhao et al., 2022a; Zhou et al., 2020). Fig. 6a shows that the addition of 0.5 g L^{-1} ferrihydrite resulted in the removal of 58.3% of Cd (initial concentration of 5 mg L^{-1}) after 24 h, and the concentration of aqueous Cd stabilized at 2.1 ± 0.1 mg L^{-1}. The long-time UV irradiation slightly improved the adsorption of Cd on ferrihydrite, likely due to a slight increase in temperature. Note that the presence of sulfite at concentrations from 2 to 10 mM SO_3^{2-} substantially abated the concentration of Cd in the aquatic phase by ~90% (Fig. 6b–d). The promoted Cd adsorption was attributed to the formation of Cd–SO_3 ternary surface complexes on the Fe(III) oxyhydroxides, which is in line with previous observations and evidenced by the increasing intensity of the FTIR peak (at ~1115 cm^{-1}) with the increase in the sulfite concentration (Fig. S7) (Zhang and Peak 2007). However, Cd adsorbed by ferrihydrite was released again as a consequence of mineral transformation under UV-induced reducing conditions. Fig. 6 depicts that the time-dependent evolution of Cd was clearly affected by the sulfite concentration and was closely linked to the relative proportions of secondary mineral phases. At 2 mM SO_3^{2-}, the apparent Cd release with the increasing time was observed, with the dissolved Cd content increasing from 9.0% to 30.8% over 8 h. The liberation of Cd was greatly inhibited at higher sulfite concentrations. At 10 mM SO_3^{2-}, the 8 h of reaction time only led to an increase in the concentration of dissolved Cd from 9.8% to 14.1%. The difference in the amount of Cd released can be explained by the different extents of ferrihydrite recrystallization and newly formed minerals. The observation of a higher Cd release at a lower sulfite concentration was considered to be correlated with the partial transformation of ferrihydrite to lepidocrocite, which poorly adsorbs Cd due to the low surface area (Zhou et al., 2020). A lower Cd release at increasing sulfite concentrations was attributed to the production of goethite, which exhibits a stronger capacity for Cd uptake (Shen et al., 2022). Previous studies have shown that the presence of SO_4^{2-} dramatically promoted Cd adsorption on goethite via the formation of Cd-SO_4 ternary surface complexes (Zhang and Peak 2007); this phenomenon has also been observed on ferrihydrite, but it was not as significant as goethite (Swedlund et al., 2009).

To explore Cd repartitioning in the solid Fe(III) minerals formed in the UV/sulfite systems as a function of the sulfite concentration, the contents of adsorbed Cd and structural Cd were measured by extraction using 0.4 M and 4 M HCl, respectively (Liu et al., 2016; Reddy et al., 2015). As illustrated in Fig. 6b–d, the concentration of structural Cd exhibited a positive correlation with the extent of ferrihydrite transformed to lepidocrocite and goethite, suggesting a strong association between Cd and the newly formed crystalline minerals. When the concentrations of SO_3^{2-} increased from 2 to 10 mM, the proportion of structural Cd dramatically increased from 8.2% to 35.1%. The higher fraction of structural Cd coexisted with crystalline minerals, which indicates a lower potential risk of heavy metal dissolution.

To understand the enhanced immobilization of Cd by the newly formed crystalline minerals at the molecular scale, the bonding environment of Cd was determined based on an analysis of the EXAFS spectra and their Fourier transforms (Fig. 7a,b respectively). The 8 h-treated samples in the UV/sulfite systems at different sulfite concentrations were subjected to analysis. As shown by the Cd k^2-weighted EXAFS spectra, the third oscillation in the k space appeared at ~7.2 $Å^{-1}$ for the Cd-bearing ferrihydrite sample (Zhao et al., 2022a); however, this value, associated with the transformation samples, shifted to a positive peak location with a more pronounced effect observed in the case of 10 mM SO_3^{2-} (at ~7.6 $Å^{-1}$). This indicates the inclusion of Cd into the structure of goethite during the UV/sulfite-initiated ferrihydrite transformation (Spadini et al., 1994; Zhao et al., 2022a). The shell-by-shell approach to EXAFS fitting (see the detailed parameters in Table S2) provided further evidence of the immobilization of Cd upon treatment with UV/sulfite, particularly at high sulfite concentrations. The first pronounced peak in the Fourier transform of Cd-bearing ferrihydrite occurred at $R + \Delta R$ = ~1.6 Å (uncorrected for phase shift), which is attributable to the Cd–O shell comprising approximately six O atoms on average of 2.27 ± 0.01 Å from the Cd atom, which is consistent with previously reported values (Spadini et al., 1994; Yan et al., 2021); however, the EXAFS of the transformed products showed that the Cd–O distance declined to the value of 2.24 ± 0.01–2.26 ± 0.01 Å, implying the existence of Cd-doping in the secondary mineral structure (Spadini et al., 1994). There were two other prominent backscattering peaks in the Fourier-transformed data, which were well-fitted with two Cd-Fe shells. For the untransformed sample, the first and second Cd-Fe shells had an interatomic distance of 3.23 ± 0.04 and 3.40 ± 0.04 Å, respectively, suggesting that Cd mainly existed as edge-sharing complexes (Randall et al., 1999; Yan et al., 2021). After a reaction time of 8 h under UV irradiation in the presence of 2, 5, and 10 mM SO_3^{2-}, the interatomic distance of the first and second Cd-Fe shells was in the range of 3.10 ± 0.01–3.15 ± 0.03 Å and 3.37 ± 0.02–3.40 ± 0.02 Å, respectively. The

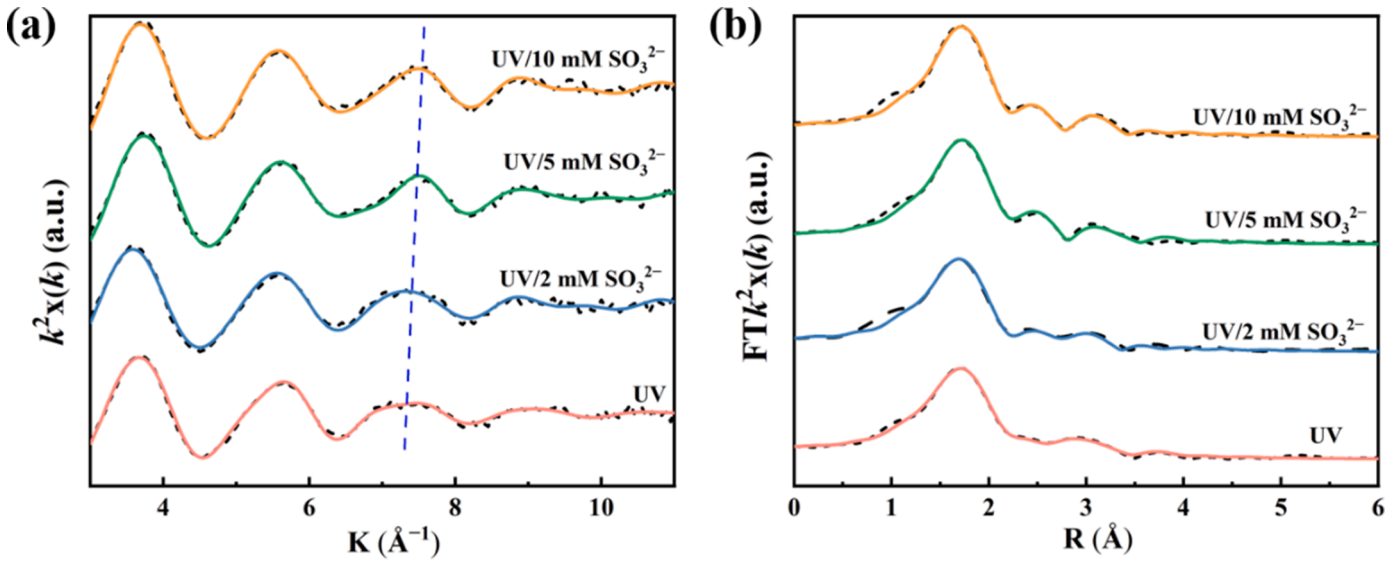

Fig. 7. (a) Cd k^2-weighted EXAFS spectra (a) and (b) their corresponding Fourier transforms of Cd-loaded ferrihydrite in the UV/sulfite systems at different sulfite concentrations. Both the measured data (dashes) and the corresponding linear combination fits (solid lines) of the EXAFS spectra are shown. Experimental conditions: [ferrihydrite] = 0.5 g L^{-1}, [Cd^{2+}] = 5 mg L^{-1}, and pH=6.8, and reaction time = 8 h.

apparent decrease, particularly in the first Cd–Fe shell, suggests that Cd was structurally doped into the secondary minerals (Zhao et al., 2022a; Zhou et al., 2020).

Moreover, the increasing aqueous sulfite concentration led to an increase in the intensity of the Cd–Fe peaks in the Fourier-transformed data. Again, this is likely to be due to the incorporation of Cd in the newly formed mineral (Burton et al., 2020; Mitsunobu et al., 2013). Likewise, the coordination number (CN) of the Cd–Fe shells significantly expanded as a result of UV/sulfite treatment and increased with higher sulfite concentrations. For example, the CN of the first Cd–Fe shell was 0.5, 1.1, 2.1, and 2.9 in relation to 0, 2, 5, and 10 mM SO_3^{2-}, respectively. This indicates that the transformation of ferrihydrite to lepidocrocite and goethite causes a tighter bonding between Cd and minerals (Burton et al., 2020). Overall, these data, in combination with the above-mentioned chemical analysis, collectively and convincingly show that Cd was incorporated into the lepidocrocite/goethite structure, possibly by replacing Fe(III).

4. Conclusions

Our findings demonstrate that the activation of aqueous sulfite by UV irradiation significantly triggered the transformation of Cd-bearing ferrihydrite to more crystalline mineral products. The concentration of sulfite added to the UV system was a key factor in determining the rate of the ferrihydrite transformation and the particular type of minerals formed. Lepidocrocite was found to be the dominant compound at a low sulfite concentration, and goethite primarily existed at a high sulfite concentration. The mechanistic studies revealed that e_{aq}^-, an extremely strong reducing species stemming from the UV/sulfite system, played an important role in driving the reduction and dissolution of ferrihydrite to Fe(II), which was subsequently adsorbed onto mineral surfaces. The amount of surface-bound Fe(II) markedly affected the transformation rate, and its oxidation by $SO_3^{\bullet-}$ was considered to be the foremost pathway governing Fe(II) conversion to newly formed Fe(III) oxyhydroxides. The combination of the chemical analysis and the Cd K-edge EXAFS analysis corroborated that an increasing proportion of Cd was more stably bound to the secondary products (particularly goethite) by structural incorporation when the photoinduced transformation occurred at high sulfite concentrations. The results strengthen our understanding of the role of photochemistry in predicting the geochemical cycle of Fe in natural environments (e.g., AMD sites) containing sulfite and thereby the fate of heavy metals that are associated with Fe minerals. Moreover, because sulfite has the benefits of abundant sources, low toxicity, and low cost, the UV/sulfite-based advanced reduction process would be a promising and viable approach to immobilize heavy metals, beyond its general recognition for eliminating a variety of persistent and toxic contaminants with high-redox potential.

Declaration of Competing Interest

The authors declare that they have no known competing financial interests or personal relationships that could have appeared to influence the work reported in this paper.

Data availability

Data will be made available on request.

Acknowledgments

We gratefully acknowledge financial support from the National Key Research and Development Program of China (nos. 2020YFC1808502 and 2018YFC1802804); the National Natural Science Foundation of China (no. U21A2034); the Guangdong Special Support Plan for Innovation Teams (no. 2019BT02L218); the Guangdong Special Support Plan for Young Top-notch Talents (no. 2019TQ05L179); the Science and Technology Planning Project of Guangdong Province, China (no. 2019A050510009); and the Natural Science Foundation of Guangdong Province, China (no. 2021B1515120077).

Supplementary materials

Supplementary material associated with this article can be found, in the online version, at doi:10.1016/j.watres.2023.119607.

References

Aeppli, M., Kaegi, R., Kretzschmar, R., Voegelin, A., Hofstetter, T.B., Sander, M., 2019. Electrochemical analysis of changes in iron oxide reducibility during abiotic ferrihydrite transformation into goethite and magnetite. Environ. Sci. Technol. 53 (7), 3568–3578.

Balistrieri, L.S., Box, S.E., Bookstrom, A.A., Ikramuddin, M., 1999. Assessing the influence of reacting pyrite and carbonate minerals on the geochemistry of drainage in the Coeur d'Alene mining district. Environ. Sci. Technol. 33 (19), 3347–3353.

Bishop, J.L., Pieters, C., Burns, R.G., 1993. Reflectance and Mössbauer spectroscopy of ferrihydrite-montmorillonite assemblages as Mars soil analog materials. Geochim. Cosmochim. Acta 57 (19), 4583–4595.

Boland, D.D., Collins, R.N., Miller, C.J., Glover, C.J., Waite, T.D., 2014. Effect of solution and solid-phase conditions on the Fe(II)-accelerated transformation of ferrihydrite to lepidocrocite and goethite. Environ. Sci. Technol. 48 (10), 5477–5485.

Burton, E.D., Hockmann, K., Karimian, N., 2020. Antimony sorption to goethite: effects of Fe(II)-catalyzed recrystallization. ACS Earth Space Chem. 4 (3), 476–487.

Burton, E.D., Hockmann, K., Karimian, N., Johnston, S.G., 2019. Antimony mobility in reducing environments: the effect of microbial iron(III)-reduction and associated secondary mineralization. Geochim. Cosmochim. Acta 245, 278–289.

Buxton, G.V., Greenstock, C.L., Helman, W.P., Ross, A.B., 1988. Critical review of rate constants for reactions of hydrated electrons, hydrogen atoms and hydroxyl radicals (•OH/•O$^-$) in aqueous solution. J. Phys. Chem. Ref. Data 17 (2), 513–886.

Chen, C., Kukkadapu, R., Sparks, D.L., 2015. Influence of coprecipitated organic matter on Fe^{2+}(aq)-catalyzed transformation of ferrihydrite: implications for carbon dynamics. Environ. Sci. Technol. 49 (18), 10927–10936.

Chen, H., Lin, T., Wang, P., Zhang, X., Jiang, F., Liu, W., 2022. Treatment of bromate in UV/sulfite autoxidation process enhances formation of dibromoacetonitrile during chlorination. Water Res. 225, 119207.

Ciani, A., Goss, K.U., Schwarzenbach, R.P., 2005. Light penetration in soil and particulate minerals. Eur. J. Soil Sci. 56 (5), 561–574.

Dong, Y., Sanford, R.A., Boyanov, M.I., Flynn, T.M., O'Loughlin, E.J., Kemner, K.M., George, S., Fouke, K.E., Li, S., Huang, D., Li, S., Fouke, B.W., 2020. Controls on iron reduction and biomineralization over broad environmental conditions as suggested by the firmicutes orenia metallireducens strain Z6. Environ. Sci. Technol. 54 (16), 10128–10140.

Druschel, G.K., Baker, B.J., Gihring, T.M., Banfield, J.F., 2004. Acid mine drainage biogeochemistry at iron mountain, California. Geochem. Trans. GT 5 (2), 13–32.

Faguy, P.W., Marinković, N.S., Adžić, R.R., 1996. Infrared spectroscopic analysis of anions adsorbed from bisulfate-containing solutions on Pt(111) electrodes. J. Electroanal. Chem. 407 (1), 209–218.

Ford, R.G., Bertsch, P.M., Farley, K.J., 1997. Changes in transition and heavy metal partitioning during hydrous iron oxide aging. Environ. Sci. Technol. 31 (7), 2028–2033.

Ford, R.G., Kemner, K.M., Bertsch, P.M., 1999. Influence of sorbate-sorbent interactions on the crystallization kinetics of nickel- and lead-ferrihydrite coprecipitates. Geochim. Cosmochim. Acta 63 (1), 39–48.

Frierdich, A.J., Beard, B.L., Reddy, T.R., Scherer, M.M., Johnson, C.M., 2014. Iron isotope fractionation between aqueous Fe(II) and goethite revisited: new insights based on a multi-direction approach to equilibrium and isotopic exchange rate modification. Geochim. Cosmochim. Acta 139, 383–398.

Gotić, M., Musić, S., 2007. Mössbauer, FT-IR and FE SEM investigation of iron oxides precipitated from $FeSO_4$ solutions. J. Mol. Struct. 834, 445–453.

Handler, R.M., Beard, B.L., Johnson, C.M., Scherer, M.M., 2009. Atom exchange between aqueous Fe(II) and goethite: an Fe isotope tracer study. Environ. Sci. Technol. 43 (4), 1102–1107.

Hansel, C.M., Benner, S.G., Fendorf, S., 2005. Competing Fe(II)-induced mineralization pathways of ferrihydrite. Environ. Sci. Technol. 39 (18), 7147–7153.

Hiemstra, T., 2013. Surface and mineral structure of ferrihydrite. Geochim. Cosmochim. Acta 105, 316–325.

Hua, J., Fei, Y.h., Feng, C., Liu, C., Liang, S., Wang, S.L., Wu, F., 2022. Anoxic oxidation of As(III) during Fe(II)-induced goethite recrystallization: evidence and importance of Fe(IV) intermediate. J. Hazard. Mater. 421, 126806.

Huang, G.X., Wang, C.Y., Yang, C.W., Guo, P.C., Yu, H.Q., 2017. Degradation of bisphenol a by peroxymonosulfate catalytically activated with $Mn_{1.8}Fe_{1.2}O_4$ nanospheres: synergism between Mn and Fe. Environ. Sci. Technol. 51 (21), 12611–12618.

Huang, J., Jones, A., Waite, T.D., Chen, Y., Huang, X., Rosso, K.M., Kappler, A., Mansor, M., Tratnyek, P.G., Zhang, H., 2021. Fe(II) redox chemistry in the environment. Chem. Rev. 121 (13), 8161–8233.

Jones, A.M., Collins, R.N., Waite, T.D., 2017. Redox characterization of the Fe(II)-catalyzed transformation of ferrihydrite to goethite. Geochim. Cosmochim. Acta 218, 257–272.
Kahani, S.A., Jafari, M., 2009. A new method for preparation of magnetite from iron oxyhydroxide or iron oxide and ferrous salt in aqueous solution. J. Magn. Magn. Mater. 321 (13), 1951–1954.
Kong, L., He, M., Hu, X., 2016. Rapid photooxidation of Sb(III) in the presence of different Fe(III) species. Geochim. Cosmochim. Acta 180, 214–226.
Larsen, O., Postma, D., 2001. Kinetics of reductive bulk dissolution of lepidocrocite, ferrihydrite, and goethite. Geochim. Cosmochim. Acta 65 (9), 1367–1379.
Lewis, D.G., Farmer, V.C., 1986. Infrared absorption of surface hydroxyl groups and lattice vibrations in lepidocrocite (γ-FeOOH) and boehmite (γ-AlOOH). Clay Min. 21 (1), 93–100.
Li, G.X., Bao, P., 2021. Transcriptomics analysis of the metabolic mechanisms of iron reduction induced by sulfate reduction mediated by sulfate-reducing bacteria. FEMS Microbiol. Ecol. 97 (3), fiab005.
Li, X., Ma, J., Liu, G., Fang, J., Yue, S., Guan, Y., Chen, L., Liu, X., 2012. Efficient reductive dechlorination of monochloroacetic acid by sulfite/UV process. Environ. Sci. Technol. 46 (13), 7342–7349.
Liang, S., Zhu, L., Hua, J., Duan, W., Yang, P.T., Wang, S.L., Wei, C., Liu, C., Feng, C., 2020. Fe^{2+}/HClO reaction produces $Fe^{IV}O^{2+}$: an enhanced advanced oxidation process. Environ. Sci. Technol. 54 (10), 6406–6414.
Liu, C., Massey, M.S., Latta, D.E., Xia, Y., Li, F., Gao, T., Hua, J., 2021a. Fe(II)-induced transformation of iron minerals in soil ferromanganese nodules. Chem. Geol. 559, 119901.
Liu, C., Zhu, Z., Li, F., Liu, T., Liao, C., Lee, J.-.J., Shih, K., Tao, L., Wu, Y., 2016. Fe(II)-induced phase transformation of ferrihydrite: the inhibition effects and stabilization of divalent metal cations. Chem. Geol. 444, 110–119.
Liu, H., Li, P., Zhu, M., Wei, Y., Sun, Y., 2007. Fe(II)-induced transformation from ferrihydrite to lepidocrocite and goethite. J. Solid State Chem. 180 (7), 2121–2128.
Liu, L., Guo, D., Ning, Z., Liu, C., Qiu, G., 2021b. Solar irradiation induced oxidation and adsorption of arsenite on natural pyrite. Water Res. 203, 117545.
Liu, T., Wang, Y., Liu, C., Li, X., Cheng, K., Wu, Y., Fang, L., Li, F., Liu, C., 2020. Conduction band of hematite can mediate cytochrome reduction by Fe(II) under dark and anoxic conditions. Environ. Sci. Technol. 54 (8), 4810–4819.
Lohmayer, R., Kappler, A., Losekann-Behrens, T., Planer-Friedrich, B., 2014. Sulfur species as redox partners and electron shuttles for ferrihydrite reduction by Sulfurospirillum deleyianum. Appl. Environ. Microbiol. 80 (10), 3141–3149.
Lovley, D.R., 1997. Microbial Fe(III) reduction in subsurface environments. FEMS Microbiol. Rev. 20 (3), 305–313.
Lv, Y., Liu, J., Zhu, R., Zhu, J., Chen, Q., Liang, X., He, H., 2022. Photoreductive dissolution of iron (hydr)oxides and its geochemical significance. ACS Earth Space Chem. 6 (4), 811–829.
Ma, S., Banfield, J.F., 2011. Micron-scale Fe^{2+}/Fe^{3+}, intermediate sulfur species and O_2 gradients across the biofilm–solution–sediment interface control biofilm organization. Geochim. Cosmochim. Acta 75 (12), 3568–3580.
Maillot, F., Morin, G., Wang, Y., Bonnin, D., Ildefonse, P., Chaneac, C., Calas, G., 2011. New insight into the structure of nanocrystalline ferrihydrite: EXAFS evidence for tetrahedrally coordinated iron(III). Geochim. Cosmochim. Acta 75 (10), 2708–2720.
Meng, F., Bu, H., Fei, Y., Chen, M., Lei, Q., Liu, D., Hua, J., Wu, F., Liu, C., 2022. Effects of clay minerals on Fe^{2+}-induced phase transformation of ferrihydrite. Appl. Geochem. 144, 105401.
Michel, F.M., Ehm, L., Antao, S.M., Lee, P.L., Chupas, P.J., Liu, G., Strongin, D.R., Schoonen, M.A.A., Phillips, B.L., Parise, J.B., 2007. Structure of ferrihydrite, a nanocrystalline material. Sci. (Am. Assoc. Adv. Sci.) 316 (5832), 1726–1729.
Mitsunobu, S., Muramatsu, C., Watanabe, K., Sakata, M., 2013. Behavior of antimony(V) during the transformation of ferrihydrite and its environmental implications. Environ. Sci. Technol. 47 (17), 9660–9667.
Pedersen, H.D., Postma, D., Jakobsen, R., Larsen, O., 2005. Fast transformation of iron oxyhydroxides by the catalytic action of aqueous Fe(II). Geochim. Cosmochim. Acta 69 (16), 3967–3977.
Qafoku, O., Kovarik, L., Bowden, M.E., Nakouzi, E., Sheng, A., Liu, J., Pearce, C.I., Rosso, K.M., 2020. Nanoscale observations of Fe(II)-induced ferrihydrite transformation. Environ. Sci. Nano 7 (10), 2953–2967.
Randall, S.R., Sherman, D.M., Ragnarsdottir, K.V., Collins, C.R., 1999. The mechanism of cadmium surface complexation on iron oxyhydroxide minerals. Geochim. Cosmochim. Acta 63 (19), 2971–2987.
Reddy, T.R., Frierdich, A.J., Beard, B.L., Johnson, C.M., 2015. The effect of pH on stable iron isotope exchange and fractionation between aqueous Fe(II) and goethite. Chem. Geol. 397, 118–127.
Saalfield, S.L., Bostick, B.C., 2009. Changes in iron, sulfur, and arsenic speciation associated with bacterial sulfate reduction in ferrihydrite-rich systems. Environ. Sci. Technol. 43 (23), 8787–8793.
Sánchez España, J., López Pamo, E., Santofimia, E., Aduvire, O., Reyes, J., Barettino, D., 2005. Acid mine drainage in the Iberian Pyrite Belt (Odiel river watershed, Huelva, SW Spain): geochemistry, mineralogy and environmental implications. Appl. Geochem. 20 (7), 1320–1356.
Schoepfer, V.A., Lindsay, M.B.J., 2022. Repartitioning of co-precipitated Mo(VI) during Fe(II) and S(-II) driven ferrihydrite transformation. Chem. Geol. 610, 121075.
Schwertmann, U., Cornell, R.M., 2008. Iron Oxides in the laboratory: Preparation and Characterization. Wiley-VCH.
Shen, X., Zhu, H., Wang, P., Zheng, L., Hu, S., Liu, C., 2022. Mechanistic and modeling insights into the immobilization of Cd and organic carbon during abiotic transformation of ferrihydrite induced by Fe(II). J. Hazard. Mater. 436, 129216.
Sheng, A., Li, X., Arai, Y., Ding, Y., Rosso, K.M., Liu, J., 2020a. Citrate controls Fe(II)-catalyzed transformation of ferrihydrite by complexation of the labile Fe(III) intermediate. Environ. Sci. Technol. 54 (12), 7309–7319.
Sheng, A., Liu, J., Li, X., Qafoku, O., Collins, R.N., Jones, A.M., Pearce, C.I., Wang, C., Ni, J., Lu, A., Rosso, K.M., 2020b. Labile Fe(III) from sorbed Fe(II) oxidation is the key intermediate in Fe(II)-catalyzed ferrihydrite transformation. Geochim. Cosmochim. Acta 272, 105–120.
Shi, M., Min, X., Ke, Y., Lin, Z., Yang, Z., Wang, S., Peng, N., Yan, X., Luo, S., Wu, J., Wei, Y., 2021. Recent progress in understanding the mechanism of heavy metals retention by iron (oxyhydr)oxides. Sci. Total Environ. 752, 141930.
Shu, Z., Liu, L., Tan, W., Suib, S.L., Qiu, G., Yang, X., Zheng, L., Liu, F., 2019. Solar irradiation induced transformation of ferrihydrite in the presence of aqueous Fe^{2+}. Environ. Sci. Technol. 53 (15), 8854–8861.
Sim, M.S., Paris, G., Adkins, J.F., Orphan, V.J., Sessions, A.L., 2017. Quantification and isotopic analysis of intracellular sulfur metabolites in the dissimilatory sulfate reduction pathway. Geochim. Cosmochim. Acta 206, 57–72.
Spadini, L., Manceau, A., Schindler, P.W., Charlet, L., 1994. Structure and stability of Cd^{2+} surface complexes on ferric oxides: 1. results from EXAFS spectroscopy. J. Colloid Interface Sci. 168 (1), 73–86.
Swedlund, P.J., Webster, J.G., Miskelly, G.M., 2009. Goethite adsorption of Cu(II), Pb(II), Cd(II), and Zn(II) in the presence of sulfate: properties of the ternary complex. Geochim. Cosmochim. Acta 73 (6), 1548–1562.
ThomasArrigo, L.K., Byrne, J.M., Kappler, A., Kretzschmar, R., 2018. Impact of organic matter on iron(II)-catalyzed mineral transformations in ferrihydrite–organic matter coprecipitates. Environ. Sci. Technol. 52 (21), 12316–12326.
Wacławek, S., Ma, X., Sharma, V.K., Xiao, R., O'Shea, K.E., Dionysiou, D.D., 2022. Making waves: defining advanced reduction technologies from the perspective of water treatment. Water Res. 212, 118101.
Wang, J., Liu, J., Peng, X., He, M., Hu, X., Zhao, J., Zhu, F., Yang, X., Kong, L., 2022. Reductive removal of As(V) and As(III) from aqueous solution by the UV/sulfite process: recovery of elemental arsenic. Water Res. 223, 118981.
Xiao, W., Jones, A.M., Collins, R.N., Bligh, M.W., Waite, T.D., 2017. Use of fourier transform infrared spectroscopy to examine the Fe(II)-catalyzed transformation of ferrihydrite. Talanta 175, 30–37.
Xiao, W., Jones, A.M., Li, X., Collins, R.N., Waite, T.D., 2018. Effect of Shewanella oneidensis on the kinetics of Fe(II)-catalyzed transformation of ferrihydrite to crystalline iron oxides. Environ. Sci. Technol. 52 (1), 114–123.
Xing, G., Garg, S., Waite, T.D., 2019. Is superoxide-mediated Fe(III) reduction important in sunlit surface waters? Environ. Sci. Technol. 53 (22), 13179–13190.
Yan, X., Zhu, M., Li, W., Peacock, C.L., Ma, J., Wen, H., Liu, F., Zhou, Z., Zhu, C., Yin, H., 2021. Cadmium isotope fractionation during adsorption and substitution with iron (oxyhydr)oxides. Environ. Sci. Technol. 55 (17), 11601–11611.
Yang, L., He, L., Xue, J., Ma, Y., Shi, Y., Wu, L., Zhang, Z., 2020. UV/SO_3^{2-} based advanced reduction processes of aqueous contaminants: current status and prospects. Chem. Eng. J. 397, 125412.
Zhang, G.Y., Peak, D., 2007. Studies of Cd(II)–sulfate interactions at the goethite–water interface by ATR-FTIR spectroscopy. Geochim. Cosmochim. Acta 71 (9), 2158–2169.
Zhao, X., Yuan, Z., Wang, S., Pan, Y., Chen, N., Tunc, A., Cheung, K., Alparov, A., Chen, W., Deevsalar, R., Lin, J., Jia, Y., 2022a. Iron(II)-activated phase transformation of Cd-bearing ferrihydrite: implications for cadmium mobility and fate under anaerobic conditions. Sci. Total Environ. 848, 157719.
Zhao, X., Yuan, Z., Wang, S., Zhang, G., Qu, S., Wang, Y., Liu, S., Pan, Y., Lin, J., Jia, Y., 2022b. The fate of co-existent cadmium and arsenic during Fe(II)-induced transformation of As(V)/Cd(II)-bearing ferrihydrite. Chemosphere 301, 134665.
Zhou, D., Chen, L., Li, J., Wu, F., 2018. Transition metal catalyzed sulfite auto-oxidation systems for oxidative decontamination in waters: a state-of-the-art minireview. Chem. Eng. J. 346, 726–738.
Zhou, S., Lai, J., Liu, X., Huang, G., You, G., Xu, Q., Yin, D., 2022. Selective conversion of biomass-derived furfuryl alcohol into n-butyl levulinate over sulfonic acid functionalized TiO_2 nanotubes. Green Energy Environ. 7 (2), 257–265.
Zhou, Z., Muehe, E.M., Tomaszewski, E.J., Lezama-Pacheco, J., Kappler, A., Byrne, J.M., 2020. Effect of natural organic matter on the fate of cadmium during microbial ferrihydrite reduction. Environ. Sci. Technol. 54 (15), 9445–9453.